First Assessment of CyGNSS-Incorporated SMAP Sea Surface Salinity Retrieval Over Pan-Tropical Ocean

Baojian Liu [ID], Wei Wan [ID], Zhizhou Guo [ID], Rui Ji, Tsechun Wang, Guoqiang Tang [ID], Yaokui Cui [ID], and Yang Hong [ID]

Abstract—In sea surface salinity (SSS) retrieval using L-band passive radiometry, radiometer-independent ocean wind speed is needed as auxiliary data. Wind speed data from scatterometer and weather models are commonly used as auxiliary data in satellite SSS missions. This article's overarching goal is to explore the feasibility of incorporating the cyclone global navigation satellite system (CyGNSS) data into the SSS retrieval algorithm of the soil moisture active and passive (SMAP) mission over tropical and subtropical oceans. As a proof-of-concept study, empirical geophysical model functions in the retrieval algorithm are developed using the statistics of collocated SMAP, CyGNSS, and referenced buoys measurements. The SSS accuracy of CyGNSS-incorporated salinity retrieval is investigated against the SMAP SSS data product. Comparisons show that the proposed CyGNSS-incorporated retrieval algorithm improves the SSS accuracy by 0.1∼0.2 psu at low wind speed (<2 m/s). To some extent, it proves that spaceborne global navigation satellite system-reflectometry (GNSS-R) could be a new and helpful data source to understand wind-induced emissivity over a smooth ocean. The dependencies of emissivity on different geophysical parameters (i.e., sea surface temperature, significant wave height, and precipitation) are analyzed, and the spatial and seasonal variabilities of SSS errors are shown and linked to these geophysical parameters. The findings of this research provide valuable insights for future development and operation of the radiometer-based SSS retrieval algorithm using wind speed data from spaceborne GNSS-R.

Index Terms—Cyclone global navigation satellite system (CyGNSS), GNSS-reflectometry, microwave radiometry, ocean salinity, ocean wind, soil moisture active and passive (SMAP).

Baojian Liu, Wei Wan, Zhizhou Guo, Rui Ji, Tsechun Wang, and Yaokui Cui are with the School of Earth and Space Sciences, Peking University, Beijing 100871, China (e-mail: liubaojian@pku.edu.cn; w.wan@pku.edu.cn; zzguo@pku.edu.cn; toplane@pku.edu.cn; 1801110642@pku.edu.cn; yaokuicui@pku.edu.cn).

Guoqiang Tang is with the Coldwater Lab, University of Saskatchewan, Canmore, AB T1W 3G1, Canada, and also with the Centre for Hydrology, University of Saskatchewan, Saskatoon, SK S7N 1K2, Canada (e-mail: guoqiang.tang@usask.ca).

Yang Hong is with the School of Civil Engineering and Environmental Science, The University of Oklahoma, Norman, OK 73019 USA (e-mail: yanghong@ou.edu).

I. INTRODUCTION

OCEAN salinity is a crucial variable in density-driven ocean circulation. Knowledge of ocean salinity is crucial for understanding the climate variability [1], water cycle [2]–[4], air-sea interactions [5], [6], and ocean biogeochemistry [7]. Remotely sensed sea surface salinity (SSS) has advantages over buoy measurements [8] in spatial and temporal coverages. Spaceborne L-band radiometry for SSS retrieval has been launched and validated in the last decade [9]. Radiometry presents its maximum sensitivity to SSS in terms of the L-band brightness temperature (T_B) [10], therefore, the accurate measurement of T_B at 1.4 GHz is significant in SSS retrieval. Missions, such as soil moisture and ocean salinity [11], Aquarius [12], soil moisture active passive (SMAP) [13], and FSSCat [14], use the radiometer to observe L-band T_B with high radiation accuracy.

Wind speed (WS) data independent of L-band radiometer measurements is essential in SSS retrieval. T_B near ocean surface is contributed by flat ocean surface brightness temperature and roughness-induced brightness temperature. The former is $T_{B,flat}$, which is a function of SSS and sea surface temperature (SST). The latter is ΔT_B, which is mainly caused by wind. It is not easy to fully separate flat surface emissivity and roughness-induced emissivity. Thus, constrained optimization algorithms are usually used to solve for salinity. WS from weather model or microwave scatterometer was used as auxiliary data in some proposed algorithms [15], [16].

SMAP was launched in January 2015 [17]. SMAP operates in a sun-synchronous orbit with an ascending node at 6 p.m. The main scientific objective of SMAP is to monitor the global soil moisture and the freeze/thaw state of the land, and SMAP observations could also be used to estimate global SSS. SSS was expected to be derived using the combined active-passive algorithm [15] with SMAP radiometer and radar used. Unfortunately, SMAP radar malfunctioned in July 2015, and WS from the National Centers for Environmental Prediction (NCEP) is used as an alternative.

Spaceborne global navigation satellite system-reflectometry (GNSS-R) is a new technique to retrieve geophysical variables cost-effectively. GNSS-R receives the reflected signal of the global navigation satellite system (GNSS) over the earth's surface, and the features of the forward-scattered signal are used to

characterize surface electromagnetic properties. Cyclone global navigation satellite system (CyGNSS) [18], launched in December 2016, has successfully used a GNSS-R constellation of 8 satellites to measure WS near cyclone eye [19]. CyGNSS data have been used in a number of ocean and land applications since its launch. For example, the assimilation of WS into numerical prediction models [20], the retrieval of soil moisture [21]–[24], the mapping of flood inundation [25], and altimetry over the ocean or lakes [26], [27].

Spaceborne GNSS-R provides new radiometry-independent WS measurements, which could be valuable in SSS retrieval. As a proof-of-concept study, this article uses the WS data from CyGNSS (the only in-orbit GNSS-R constellation with publicly available data) as prior WS in SSS retrieval. Preliminary research has shown the statistical relationship between CyGNSS WS and ocean surface emissivity increment [14], [28]–[30]. The statistics indicated that CyGNSS data had shown the potentials to improve the accuracy over the relatively smooth ocean. We incorporate the CyGNSS WS into the SSS retrieval algorithm of the SMAP mission over the tropical and subtropical ocean. Empirical geophysical model function (GMF) is parameterized using the statistics of excess brightness temperature and CyGNSS WS, and the GMF is then implemented in the retrieval of SSS. The dependencies of emissivity on different geophysical parameters (SST, significant wave height (SWH), and precipitation) are analyzed. Furthermore, the spatial and seasonal variabilities of SSS errors are shown and linked to these geophysical parameters. The findings of this study provide valuable insights for future development and operation of the radiometer-based SSS retrieval algorithm using WS data from spaceborne GNSS-R.

II. DATA AND METHODS

A. Data Sets

1) CyGNSS Data: CyGNSS measures tropical WSs between $40°$S and $40°$N with a spatial resolution of ~ 25 km. Orbiting at an inclination angle of $35°$, CyGNSS receives the reflected signal over the tropical ocean, and the on-board payloads integrate the reflected signal into $\mathrm{Delay} \times \mathrm{Doppler}$ bins, i.e., Delay–Doppler map (DDM) [31]. The WS was derived based on CyGNSS geophysical model function ($\mathrm{GMF_{WS}^{CYG}}$) [32] using DDM observable. In this article, two-year National Oceanic and Atmospheric Administration (NOAA) CyGNSS v1.1 data [34] from August 1, 2018 to July 31, 2020 are used. To develop the GMFs and evaluate the results conveniently, we use the same input geophysical variables as the benchmark. Thus, we use the L2 WS product instead of the L1 DDM, although the L1 DDM might have more potentials in the future. CyGNSS L2 provides some useful data quality labels. Pixels with a "possible low quality" flag are excluded in this study. Data with range-corrected antenna gain (RCG) [33] ≥ 20 (scaled by 10^{-27}) are used to develop excess emissivity GMF, and data with RCG > 10 are used in the following computation and validation.

2) SMAP Data: SMAP SSS data (L2, v5.0) [35] from August 1, 2018 to July 31, 2020 are used. SMAP observed horizontal and vertical (h and v) linear polarized $\mathrm{T_B}$ from two different
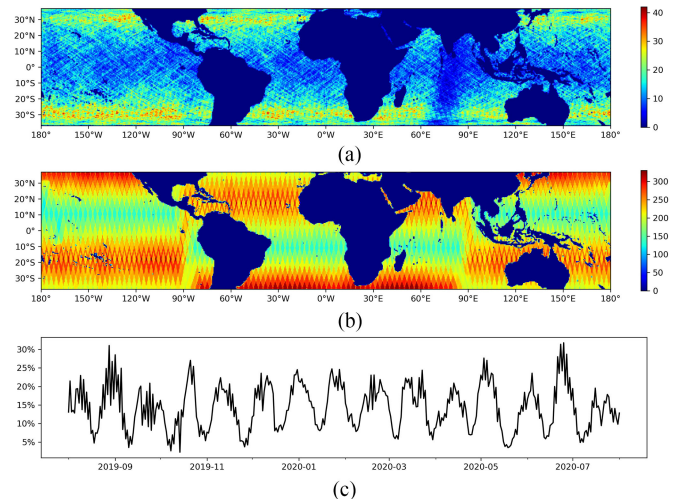

Fig. 1. Density map of the matchups. The number of days with valid data per year is binned into $0.5° \times 0.5°$ grid boxes. (a) Number of days with valid CyGNSS-SMAP matchups. (b) Number of days with valid SMAP observations. (c) Percentage of SMAP grid cells that can match up with CyGNSS per day. Grid cells only between $35°$S and $35°$E are counted.

look directions (the four combinations of polarization and "look" were often called "flavors") by mechanically rotating a 6-meter-diameter real aperture antenna. In the SMAP L1B algorithm, sources of errors such as Faraday rotation, radio frequency interference, sun glint, land effect, reflector emissivity correction, and the galactic contribution are considered. In this article, we focus on investigating the ocean surface roughness effect. SMAP L2 product is on a swath centered on the subsatellite track, with a resolution of about 60 km. $\mathrm{T_B}$ in SMAP L2A is an essential variable in the GMF parametrization and SSS retrieval. SSS in SMAP L2B ($\mathrm{SSS_{v5}}$) is used as the benchmark, and the auxiliary WS, SWH from NCEP, is used in some comparisons and discussions. SMAP and CyGNSS data are collocated temporally and spatially. A distance threshold of $\pm 0.125°$ and a time window of ± 0.5 h are used in the collocation. As shown in Fig. 1, the number of days with valid data is calculated within each $0.5° \times 0.5°$ grid cell. In most tropical and subtropical regions, there are about $150 \sim 300$ days with valid SMAP $\mathrm{T_B}$ [Fig. 1(b)]. For most grid cells, the number of CyGNSS-SMAP matchups ranges from 10 to 30 [Fig. 1(a)]. The day-by-day percentage of SMAP grid cells that can match up with CyGNSS is depicted in Fig. 1(c).

3) ARGO Data and Other Data: Array for real-time geostrophic oceanography (ARGO) data[1] is used as the ground truth. ARGO provides global ocean temperature and salinity profiles from more than 3000 buoys. Remote sensing methods can only measure the surface layer parameters of the ocean. Thus, the first layer (at ~ 5 m depth) of the ARGO profile is defined as "surface" in this study. ARGO profiles are ideal ground truth with an accuracy of 0.01 psu for salinity [36]. ARGO profiles with quality control flags set to 1 (i.e., good data) are employed. Remotely sensed data are collocated with ARGO

---

[1][Online]. Available: http://www.argo.net/

using collocation radii of ± 2 days and $\pm 0.5°$. There are about 2.4×10^5 matchups after collocated with ARGO measurements. Similar to Fig. 1(a), data density is higher in high latitude regions.

In addition, we also discuss the rain effect on the salinity. Precipitation data are from the Integrated Multi-satellitE Retrievals for GPM (IMERG) [37]. IMERG is at a spatial resolution of $0.1°$ and temporal resolution of 30 min.

B. Sea Surface Salinity Retrieval

As mentioned earlier, because it is not easy to fully separate the effect of WS from surface brightness temperature, the constrained optimization methods are commonly used in SSS retrieval. First, models are developed to estimate T_B [see Sections II.B.1–II.B. 3]. Second, the SSS is calculated by the maximum likelihood method (see Section IV).

1) Flat Ocean Surface T_B: The ocean surface T_B is simplified as the sum of flat ocean surface T_B ($T_{B,flat}^p$) and wind-induced T_B (ΔT_B^p) in SMAP SSS optimization [(1)–(5)] [13]

$$T_B^p = T_{B,flat}^p \; (SSS, SST) + \Delta T_B^p \; (WS, SWH, \phi, SST) \quad (1)$$

where p stands for horizontal or vertical polarization (h or v). SWH stands for SWH. ϕ is relative wind direction. T_B is computed using the following equations:

$$T_{B,flat}^h = \left(1 - R^h\right) \times SST \quad (2)$$

$$T_{B,flat}^v = \left(1 - R^v\right) \times SST \quad (3)$$

$$R^h = \left| \frac{\varepsilon \cos\theta - \sqrt{\varepsilon - \sin^2\theta}}{\varepsilon \cos\theta + \sqrt{\varepsilon - \sin^2\theta}} \right|^2 \quad (4)$$

$$R^v = \left| \frac{\cos\theta - \sqrt{\varepsilon - \sin^2\theta}}{\cos\theta + \sqrt{\varepsilon - \sin^2\theta}} \right|^2 \quad (5)$$

where R^h and R^v are horizontal and vertical Fresnel reflectivity, θ is the incident angle, and ε is permittivity. For SMAP, the incident angle $\theta = 40°$. SST stands for NOAA optimum interpolation SST. As a function of SSS and SST, permittivity ε is calculated using the model proposed in [10].

2) Geophysical Model Function for Wind-Induced Δe: Wind-induced ΔT_B in (1) is calculated by SST and GMF_e as follows:

$$\Delta T_B^p = SST \times \Delta e^p \left(WS, \phi, SST, SWH\right). \quad (6)$$

In SMAP SSS v5.0, wind-induced emissivity Δe^p is simulated by $GMF_{e,p}^{NCEP}$. The parameterization of SMAP SSS is similar to Aquarius [38], [39] and adapted for the NCEP ancillary data.

GNSS-R is a new technique with new designs and algorithms. We cannot simply take the GMF from scatterometers or weather models. Thus, empirical GMFs are rederived based on the statistics of collocated remote sensing and ARGO measurements. In this section, a WS-only GMF is derived using CyGNSS WS. Δe's dependence on other geophysical variables will be discussed in the following.
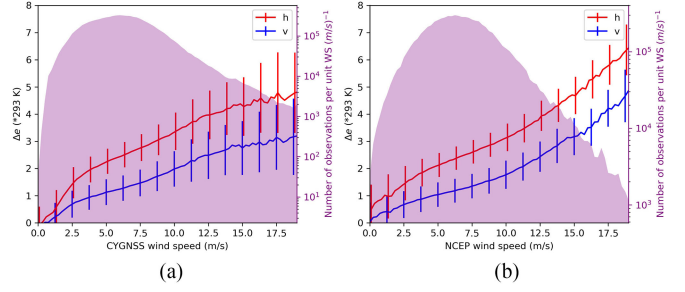

Fig. 2. Mean value and standard deviation (σ) of ΔT_B as functions of (a) CyGNSS WS and (b) NCEP WS. Red and blue lines represent horizontal and vertical polarization, respectively. The numbers of collocation data are in the purple shaded area.

GNSS-R receives forward-scattered signal near-normal specular direction so that GMFs derived from CyGNSS have some new features that need to be taken into account. These features and related considerations are as follows.

1) In GMF_{WS}^{CYG}, the root mean square error (RMSE) increases with increasing WS [40], so that CyGNSS data under high WS conditions might be unreliable in SSS retrieval [28]. At low WS, the signal-to-noise ratio (SNR) is higher, and the signal might be partially coherent. Thus, an accurate retrieval can be expected.

2) CyGNSS DDM observables, e.g., DDM average [41], are not sensitive to wind direction. Meanwhile, considering that the directional modulation of Δe is minimal for WS < 12 m/s [39], we derive an isotropic GMF without harmonic term.

$\mathbf{\Delta e^p}$ as a function of CyGNSS WS can be described as follows:

$$\Delta e^p = GMF_{e,p}^{CYG} \left(WS\right). \quad (7)$$

Empirical $\mathbf{GMF_{e,p}^{CYG}}$ is parameterized using the statistics of SMAP and CyGNSS observations as follows. CyGNSS data with RCG > 20 is used in the GMF development. Derived from (2), (3), and (6), the $\mathbf{\Delta e}$ versus WS lookup tables for h and v polarization are generated with the mean value of collocated data as follows:

$$\Delta e^h|_{WS = WS_0} = \langle \frac{T_B^h - T_{B,flat}^h}{SST} \rangle|_{WS=WS_0} \quad (8)$$

$$\Delta e^v|_{WS = WS_0} = \langle \frac{T_B^v - T_{B,flat}^v}{SST} \rangle|_{WS=WS_0} \quad (9)$$

where $\mathbf{WS_0}$ are WS bins in 0.25 m/s resolution. Subsequently, the GMF is populated by linear interpolation. In Fig. 2(a), the mean value and standard deviation (σ) of $\mathbf{\Delta T_B^h}$ and $\mathbf{\Delta T_B^v}$ as functions of CyGNSS WS ($\mathbf{WS_{CYG}}$) are shown. As a comparison, the dependence of $\mathbf{\Delta T_B}$ on NCEP WS ($\mathbf{WS_{NCEP}}$) is illustrated in Fig. 2(b). Note that $\mathbf{\Delta e}$ in Fig. 2 is converted to $\mathbf{\Delta T_B}$ by multiplying 293 K for readability. The same conversions are performed in the below-mentioned figures.

It can be concluded from Fig. 2:

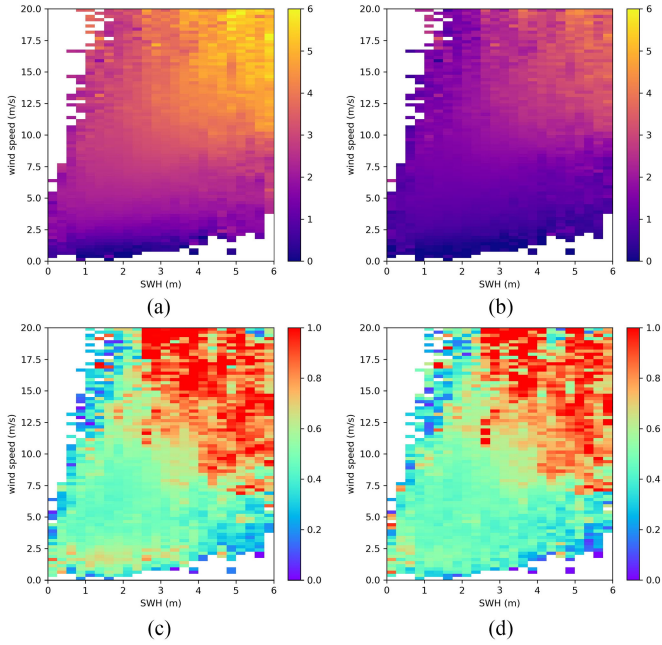1) The peak of WS density is near 6 m/s in collocated data sets.

Fig. 3. 2-D GMF of $\mathbf{\Delta e}$ as a function of CyGNSS WS and SWH. The mean values and standard deviations (σ) of $\mathbf{\Delta e}$ are shown. (a) Mean values of $\mathbf{\Delta e^h}$. (b) Mean values of $\mathbf{\Delta e^v}$. (c) σ of $\mathbf{\Delta e^h}$. (d) σ of $\mathbf{\Delta e^v}$.
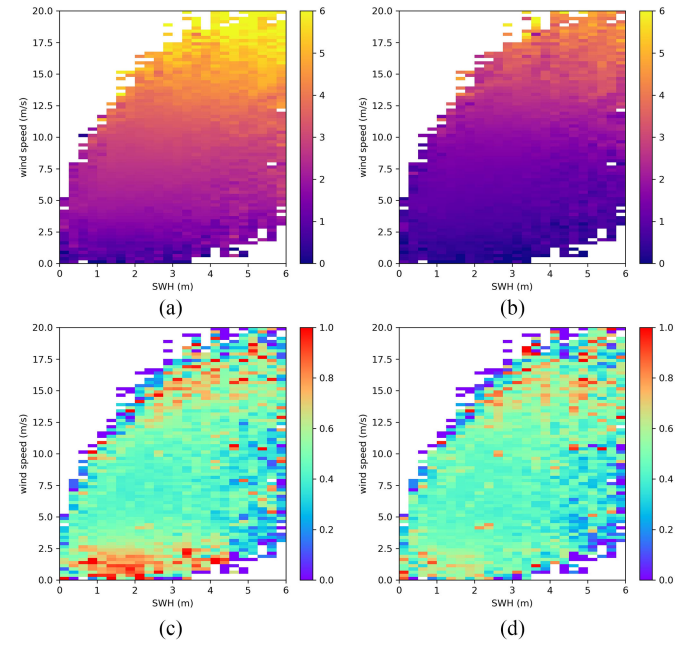

Fig. 4. Same statistics as Fig. 3 for NCEP WS. (a) Mean values of $\mathbf{\Delta e^h}$. (b) Mean values of $\mathbf{\Delta e^v}$. (c) σ of $\mathbf{\Delta e^h}$. (d) σ of $\mathbf{\Delta e^v}$.

2) The Δe of CyGNSS and NCEP diverge when WS > ~12 m/s.

3) The CyGNSS Δe has zero means when WS < 0.5 m/s for both h and v polarizations, consistent with known GMFs. It does not mean CyGNSS measures the true WS more accurately. For a given WS_{NCEP} with a near-zero value, the presence of swell might prevent the surface from completely smooth [38], [42]. In contrast, CyGNSS might measure the actual roughness of the surface. So, the measurements of CyGNSS agree better with SMAP's roughness-driven emissivity.

4) CyGNSS GMF has similar $\sigma_{\Delta e}$ to NCEP at low and moderate WS ($\sim$ < 10 m/s). At high WS, the $\sigma_{\Delta e}$ of CyGNSS increases with increasing speed and becomes much larger than the NCEP $\sigma_{\Delta e}$. CyGNSS was designed with a baseline requirement of 10% uncertainty when WS > 20 m/s. So, as expected, the $\sigma_{\Delta e}$ is large at high WS.

3) Δe's Dependence on Other Variables: In addition to WS, geophysical parameters, such as SST, SWH, and precipitation, are able to affect Δe. In this section, Δe's dependences on these parameters are incorporated in the forward model.

For the SWH-induced roughness correction, Δe^h and Δe^v are averaged into two-dimensional (2-D) (CyGNSS WS and SWH) intervals, then the lookup tables are populated by bilinear interpolation. The statistics of Δe, calculated using GMF_{2-D} defined in (10), within the 2-D intervals are shown in Fig. 3 ($*293$ K for readability). As a comparison, the same statistics as functions of NCEP WS are shown in Fig. 4.

$$\Delta e^p = GMF_{2-D,p} \ (WS, \ SWH) \tag{10}$$

where p stands for h or v.

As seen in Fig. 3(a) and (b), at high CyGNSS WS, the SWH dependencies of Δe are strong. The SWH contains essential information of Δe when WS > 9 m/s. With the variation of SWH, the range of Δe^h can be more than 3 K at a specific WS. This is different from NCEP WS in Fig. 4(a) and (b) and some previous research [13], [39], [42].

The standard deviations ($\sigma(\Delta e^h)$ and $\sigma(\Delta e^v)$) affect the accuracy of SSS retrieval below. As shown in Fig. 3, in high WS and large SWH conditions, the stand deviations are large. The trend is consistent with Fig. 2, but the 2-D comparison shows more details than Fig. 2. The inaccuracy starts from CyGNSS WS > 7 m/s and NCEP SWH > 2 m. If either the WS or the SWH is lower than the threshold, the σ of Δe will be less than ~0.5 K.

At low WS (< 2 m/s), CyGNSS WS performs better. The standard deviations of Δe_h and Δe_v are smaller than those in Fig. 4(c) and (d). Especially for the standard deviations of Δe_h, the NCEP's 2-D GMF shows its maximum RMSE (up to 1.0 K) when WS < 2.5 m/s. In the 2-D comparison, advantage in RMSE at low WS is more evident than the 1-D GMF.

We speculate as to the explanations for the features of GMF_{2-D}. The first is about the high-WS performance. When the waves are breaking or broken with the increasing WS, Δe of the L-band is sensitive to the whitecaps [43]. However, whitecaps have not been considered in theoretical and empirical GNSS-R GMFs [31], [33], [44]. The wave dependency of Δe at high CyGNSS WS indicates that the large uncertainty of Δe might not be attributed only to the CyGNSS's designed 10% baseline accuracy. GNSS-R might not capture the whitecaps in the process of wave breaking. Therefore, the GMF looks different from Fig. 4.
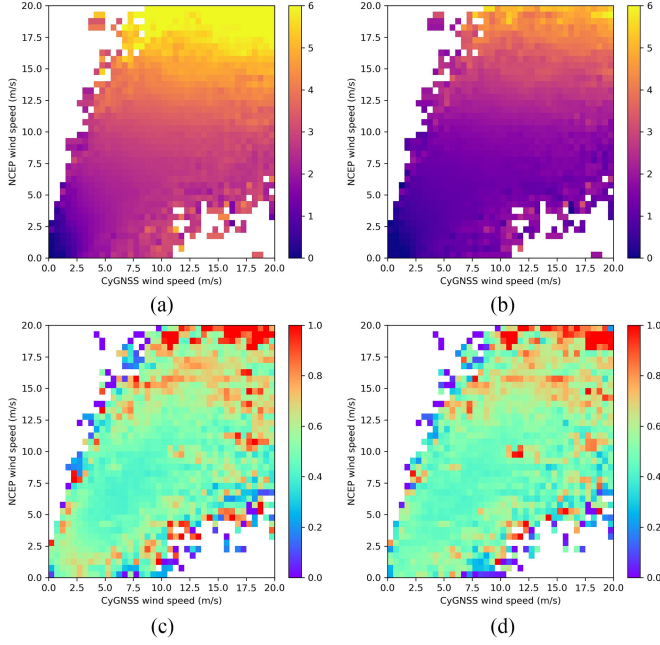
Fig. 5. Combined GMF of $\Delta\mathbf{e}$ with CyGNSS WS and NCEP WS as inputs. The statistical variables shown are same as Figs. 3 and 4.

The second is about the low-WS performance of CyGNSS. Same as Section II.B.2, CyGNSS might measure the actual roughness at low WS. Fig. 2 shows that CyGNSS-based GMF has a more accurate mean Δe value, and Figs. 3 and 4 show that the RMSE is also better.

Similarly, a combined GMF (GMF_{comb}), defined in (11) is developed experimentally with two WS sources (WS_{CYG} and WS_{NCEP}) as inputs.

$$\Delta e^p = GMF_{comb,p} \left(WS_{CYG}, WS_{NCEP}\right). \quad (11)$$

As will be shown in Section III.B, WS_{CYG} and WS_{NCEP} are correlated with a correlation coefficient (CC) greater than 0.8, which is inevitable because they are the same geophysical variable. Nevertheless, Fig. 5(a) and (b) show that when WS_{CYG} and WS_{NCEP} disagree with each other, the Δe^p differs from the emissivity near the 1:1 line. At low WS, the WS_{CYG} dominated the Δe^p, whereas the WS_{NCEP} dominated the Δe^p at high WS. The GMF_{comb} has a relatively low $\sigma(\Delta e^p)$ under a broader WS range. Thus, GMF_{comb} may combine the advantage of both WS, and avoid the worse result of either single-input GMF.

The rain-induced Δe and the SST-dependence of Δe cannot be readily described mathematically. The effects of them are usually empirical and not evident. In SMAP SSS v5.0, the rain effect of Δe is not corrected. Therefore, results are also without rain effect correction in this article.

We take the same approach as SMAP SSS [39] to correct the SST effect on the Δe. The wind-driven Δe is assumed proportional to the emissivity; therefore, the Δe is SST-dependent as follows:

$$\Delta e^p_{SST} = \Delta e^p \frac{e^p(T_{ref})}{e^p(SST)}, \quad T_{ref} = 20° \text{ C.} \quad (12)$$

TABLE I
SYMBOL, THE GMF USED, AND THE INPUTS OF THE ALGORITHMS

Symbol	GMF	Inputs
SSS_{v5}	SMAP GMF	NCEP WS, SWH, wind direction, SST
SSS_{CYG}	Equation (7)	CYGNSS WS, SST
SSS_{CYG2}	Equation (10)	CYGNSS WS, SWH, SST
SSS_{comb}	Equation (11)	CYGNSS WS, NCEP WS, SST

4) Constrained Optimization: With WSs as auxiliary data, SMAP L2B retrieves SSS and WS by a maximum likelihood algorithm with objective function as follows:

$$F (\mathbf{SSS}, \mathbf{WS})$$
$$= \sum_i \left[\frac{\mathbf{T_{B,}}_i - \mathbf{T_{B,}}_i^m (\mathbf{SSS}, \mathbf{SST}, \mathbf{WS}, \mathbf{SWH}, \phi)}{\mathbf{NEDT}_i}\right]^2$$
$$+ \left[\frac{\mathbf{WS} - \mathbf{WS_a}}{\delta_{\mathbf{ws}}}\right]^2 \quad (13)$$

where i is one of the four flavors (i.e., H-aft, V-aft, H-fore, V-fore). $\mathbf{T_{B,}}_i$ is SMAP L2A $\mathbf{T_B}$ measurements at one of the four flavors. $\mathbf{T_{B,}}_i^m$ stands for modeled $\mathbf{T_B}$ in (1) as a function of SSS, SST, WS, SWH, and ϕ (ϕ is not included in $\mathbf{GMF_{e,p}^{CYG}}$). NEDT is the noise-equivalent delta $\mathbf{T_B}$ in SMAP L2A. $\mathbf{WS_a}$ is ancillary WS ($\mathbf{WS_{NCEP}}$ or $\mathbf{WS_{CYG}}$ in this study), $\delta_{\mathbf{ws}}$ is a priori standard deviation on WS and $\delta_{\mathbf{ws}} = 1.5 \text{ m/s}$. Constrained optimizations in this study are solved in [45].

With the permittivity model, GMF [(7)–(12)], and objective function [(13)] earlier, SSS could be retrieved using collocated SMAP T_B and CyGNSS WS. CyGNSS observations with RCG > 10 are used in the retrieval. The SSS results compared in Section III are listed in Table I. The symbols, the GMF used, and the inputs of the algorithms are detailed in Table I.

III. RESULTS AND DISCUSSION

A. Wind Speed Effect

The difference between satellite salinity (SSS_{RS}) and ARGO salinity (SSS_{ARGO}) is the most significant indicator to evaluate the accuracy of SSS retrieval. The mean difference between SSS_{RS} and SS_{ARGO} (i.e., the bias) and the RMSE of SSS_{RS} are shown in Fig. 6. Rain-free data (rain rate < 0.1 mm/h) are used in the comparison. SSS_{RS} based on four different GMFs are compared. SSS_{v5} is the salinity in SMAP v5; SSS_{CYG} is based on GMF_{CYG}, the WS-only GMF in Section II.B.2); SSS_{CYG2} is based on GMF_{2D}, the 2-D GMF in Section II.B.3); SSS_{comb} is based on GMF_{comb}, the combined GMF in Section II.B.3). In Fig. 6, the RMSE increases with WS, consistent with the GMF figures earlier. The RMSE is smaller than ~ 0.75 psu when WS < 9 m/s (70.4% of all). Since the accuracy of SSS retrieval is quite low when $\sigma > 0.75$, hereafter the threshold is set to 9 m/s to exclude the low-quality SSS_{CYG}.

At low WS, different CyGNSS-incorporated algorithms have no significant difference, and they are more accurate than SSS_{v5}. In Fig. 6, the mean of SSS_{CYG} is more accurate by 0.1∼0.2 psu
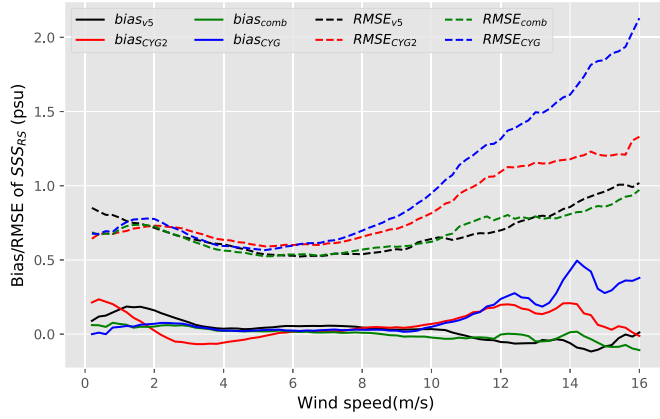
Fig. 6.   Bias and RMSE of $\mathbf{SSS_{RS}}$ at different WSs. Only rain-free data (rain rate< 0.1 mm/h) are exhibited.

Fig. 7.   Overall accuracies of auxiliary WS, $\mathbf{SSS_{CYG2}}$, and $\mathbf{SSS_{v5}}$. (a) Difference between CyGNSS WS and NCEP WS. (b) Difference between SMAP v5.0 SSS ($\mathbf{SSS_{v5}}$) and ARGO SSS. (c) Difference between CyGNSS-incorporated SSS and ARGO SSS. (d) $\mathbf{SSS_{CYG2}}$ versus $\mathbf{SSS_{ARGO}}$ after excluding WS > 9 m/s data.

than $\mathrm{SSS_{v5}}$ only when WS is very low (WS < 2 m/s), with the p-values of the F-test less than 0.01. The RMSE differences of $\mathrm{SSS_{v5}}$ and $\mathrm{SSS_{CYG2}}$ are 0.37, 0.12, and 0.09 psu at 0∼0.5, 0.5∼1, and 1∼1.5 m/s, respectively.

At high WS, the NCEP-incorporated algorithms are better than those NCEP-independent. The incorporation of SWH can reduce the gap but cannot inverse this trend. At high WS, $\mathrm{SSS_{comb}}$ is more accurate than $\mathrm{SSS_{CYG2}}$, with the p-values of the F-test < 0.01 only when WS>2.5 m/s. The RSME of $\mathrm{SSS_{comb}}$ is 0.14 psu smaller than $\mathrm{SSS_{CYG2}}$ at 9 m/s, and 0.26 psu smaller at 15 m/s. When WS>10 m/s, the $\mathrm{SSS_{CYG}}$ and $\mathrm{SSS_{CYG2}}$ suffer a positive bias, and the bias increases with the increasing WS for $\mathrm{SSS_{CYG}}$. Only $\mathrm{SSS_{CYG2}}$ will be compared in the discussions hereafter, because the RMSE is better than that of $\mathrm{SSS_{CYG}}$ in a wider WS range and it is independent of NCEP WS.

The higher accuracy of $\mathrm{SSS_{CYG2}}$ at low WS can be attributed to CyGNSS data's high SNR over a smoother surface. CyGNSS's reflection is partially coherent over the smooth surface [46], which might improve the accuracy of GMF. In addition, studies have reported that the swell effect is noticeable in CyGNSS when the wind-driven roughness is mild [47], [48]. Similarly, the swell-driven ΔT_B is measurable only when the WS is low for the L-band radiometer. The similarity might cause the better performance of CyGNSS at low WS.

The overall accuracies of auxiliary WS and SSS retrieval are shown in Fig. 7. The bias between $\mathrm{WS_{CYG}}$ and $\mathrm{WS_{NCEP}}$ is 0.40 ± 1.67 m/s in Fig. 3(a), and the bias between $\mathrm{SSS_{v5}}$ and $\mathrm{SSS_{ARGO}}$ is 0.04 ± 0.59 psu in Fig. 3(b). The accuracy of v5.0 SSS is higher than SMAP SSS v4.2 [28]. As shown in Fig. 3(c) and (d), the overall accuracy of $\mathrm{SSS_{CYG2}}$ ($\sigma = 0.69$ psu) is worse than $\mathrm{SSS_{v5}}$ ($\sigma = 0.59$ psu). The accuracy of $\mathrm{SSS_{CYG2}}$ is significantly improved ($\sigma = 0.62$ psu) when filtering out the WS > 9 m/s data. The $\mathrm{SSS_{v5}}$ is improved quite a little under the same filtering [not shown for its similar look to Fig. 3(b)].
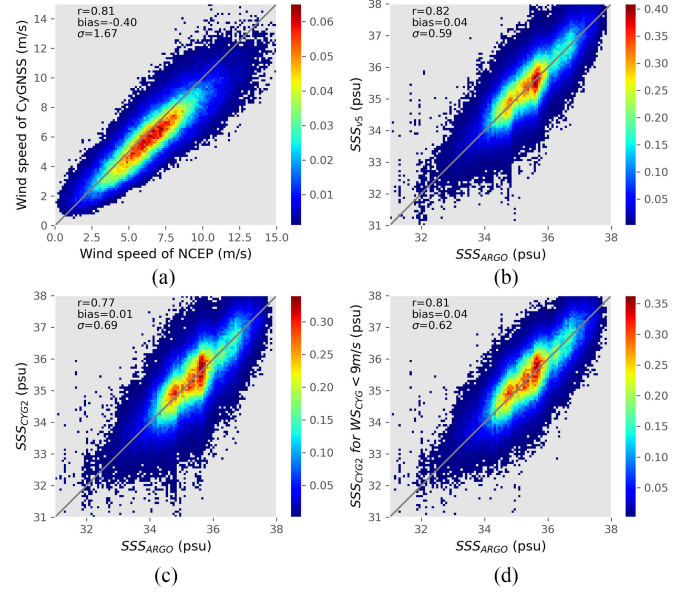
B. Effects of SST, SWH, and Precipitation

An inter-comparison is made to understand the contributions of different geophysical variables on SSS error. As shown in Section II.B and some previous studies [39], [42], [49]–[51], SST and SWH are usually less significant than WS in the Δe correction, so the residuals of SSS retrieval are used to present Δe's dependence on these parameters. In order to separate the impact of some correlated variables (SWH and SST), some statistics are made by binning SSS residuals into 2-D intervals.

The joint effect of SWH and SST on SSS residuals is shown in Fig. 8. The CC between SWH and SST equals -0.42 for WS < 9 m/s, the absolute value of which is greater than those between SWH and WS (0.24 for $\mathrm{WS_{NCEP}}$ and 0.33 for $\mathrm{WS_{CYG}}$). Thus, it is necessary to rank the importance of SST and SWH. As shown in Fig. 8(b) and (e), the RMSE decreases with increasing SST for both $\mathrm{SSS_{CYG2}}$ and $\mathrm{SSS_{v5}}$, which is the inevitable result of the radiometer's higher sensitivity to SSS at high SST.

In the retrieval of $\mathrm{SSS_{CYG2}}$ and $\mathrm{SSS_{v5}}$, the GMFs to correct the SWH effect are data-driven. Therefore, it is expected that the bias is independent of SWH in Fig. 8(a) and (d). It is noticeable in Fig. 8(a) and (d) that the bias of SSS depends on the SST. In $\mathrm{SSS_{v5}}$, the SSS is overestimated in a warmer ocean (SST $> 25°$C), which has been pointed out in [39]. In $\mathrm{SSS_{CYG2}}$, the salinity is overestimated when the SST $< 20°$C. The "assumption" in [39] [i.e., (12)] might be questionable and need to be improved in a broader SST range.

The rain effect on SSS retrieval is different from the other variables. The rain freshens the ocean surface, diluting the SSS directly, and the rain could also roughen the ocean surface, causing a negative bias in SSS retrieval [52]. In this research, we do not separate the roughening effect and the freshening effect.
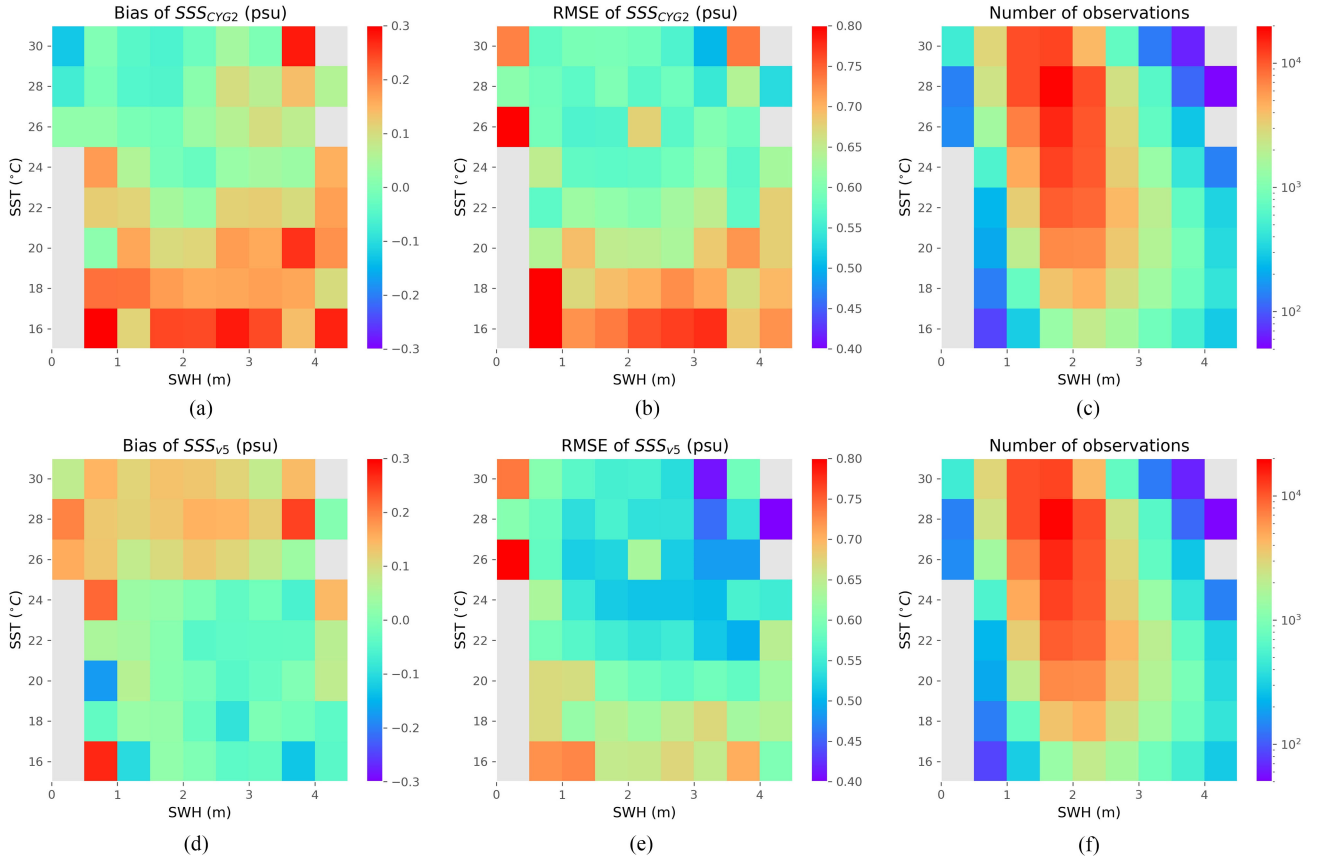
Fig. 8. Joint effect of SWH and SST on SSS uncertainty. (a) Bias of SSS_{CYG2}. (b) RMSE of SSS_{CYG2}. (c) Number of points in each 0.5 m × 2°C interval. (d) Bias of SSS_{v5}. (e) RMSE of SSS_{v5}. (f) Number of points in each 0.5 m × 2°C interval. Cells with less than 50 observations are excluded.

TABLE II
bias$_{CYG2}$ AND **bias$_{v5}$** FOR DIFFERENT IMERG RAIN RATES

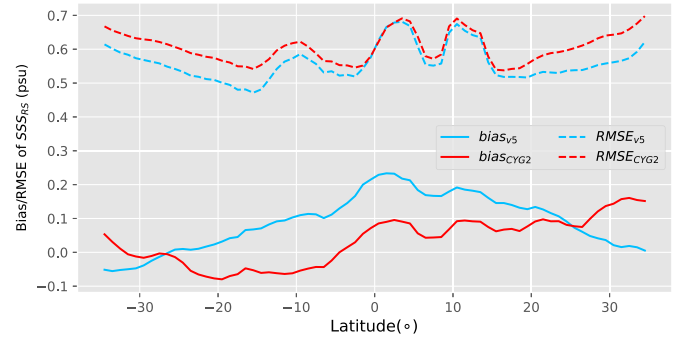| rain rate (mm/h)	bias$_{CYG2}$ (psu)	bias$_{v5}$ (psu)	Number
No rain (< 0.1)	0.04	0.06	227784
0.1~1	-0.20	-0.15	10349
1~2	-0.50	-0.49	1831
2~3	-0.71	-0.70	812
3~4	-0.87	-0.82	405
4~5	-0.96	-0.95	230
5~6	-1.17	-1.14	162
6~7	-1.31	-1.34	110
7~8	-1.57	-1.52	76
8~9	-1.46	-1.41	60
9~10	-1.62	-1.56	34

Fig. 9. Latitudinal variation of SSS uncertainties. Red and blue lines show the bias and RMSE of SSS_{CYG2} and SSS_{v5}, respectively.

Instead, we calculate the bias of SSS as a function of the IMERG rain rate in Table II, and compare them to some state-of-the-art results.

From Table II, the bias$_{CYG2}$ and bias$_{v5}$ are approximately equal, with a maximum absolute difference less than 0.05 psu. We compare the rain freshening effect $\Delta SSS/RR$ (RR is the rain rate) in this article with results in [53]. The $\Delta SSS/RR$ is about -0.16 psu $\cdot (mm/h)^{-1}$ in Table II. The value agrees exactly with the theoretical prediction (-0.15 psu $\cdot (mm/h)^{-1}$)

and other L-band experiments (range from -0.07 to -0.36 psu $\cdot (mm/h)^{-1}$). The results show that the present knowledge about the rain freshening of surface salinity is true in CyGNSS-incorporated roughness correction.

C. Spatial and Seasonal Variability of SSS Error

The detailed seasonal-latitudinal variations of SSS bias are shown in Fig. 9. The RMSE of SSS_{CYG2} is similar to SSS_{v5}. Moreover, the mean bias is ~0.1 psu closer to zero. In the tropical ocean between 10°N(S) and 20°N(S), the bias of SSS_{CYG2} is closer to zero than SSS_{v5}, but less accurate in RMSE.
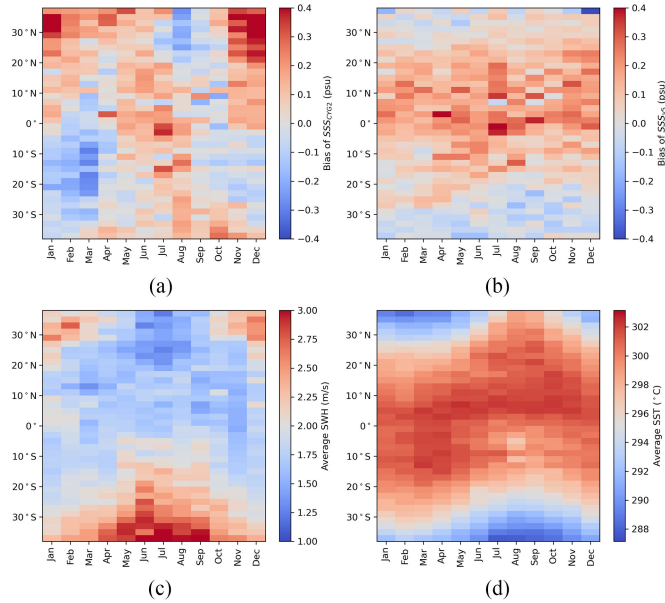
Fig. 10. SSS bias as a function of month and latitude. Data with WS below 9 m/s are used. (a) Bias of SSS_{CYG2} as a function of month and latitude. (b) Same for SSS_{v5}. (c) Hovmoller diagram of average SWH. (d) Hovmoller diagram of average SST.

In the subtropical region, the bias of SSS_{CYG2} increases with the increasing of latitude, and the RMSE is larger than SSS_{v5}.

The SSS bias as a function of month and latitude is compared with SWH and SST in Fig. 10. The bias of SSS_{CYG2} is season-dependent at high latitude. The SSS_{CYG2} overestimated the salinity in northern hemisphere winter, and the bias of SSS_{v5} is positive in the equatorial region all over the year. These results are consistent with the SST dependence in Fig. 8. The overestimations in July [see both Fig. 10(a) and (b)] are probably caused by the galactic contamination in SMAP L1B [13].

The spatial variability of SSS uncertainty is shown in Fig. 11. SSS uncertainty is binned into the $3° \times 3°$ grid and compared to SSS, SST, SWH, and WS. The spatial pattern of RMSE of SSS_{CYG2} is similar to SSS_{v5} [see Fig. 11(h) and (i)], and both of them are consistent with the knowledge earlier. The average SWH (d) and WS (e) vary with region, whereas the spatial pattern of mean SSS bias is similar to that of SST (c). Significant overestimations are observed near the west coast of North America and South America [Fig. 11(f)], where the ocean is relatively cold [Fig. 11(c)] and calm [Fig. 11(d)]. SSS_{v5} [Fig. 11(g)] with the same land correction is more accurate, so the overestimation is not caused by the land effect. The overestimation in the cold and calm ocean can be the evidence of the conclusions earlier, i.e., the best knowledge on SST correction of the Δe and should be improved.

IV. CONCLUSION

In this article, the WS data of the CyGNSS are incorporated into the SSS retrieval algorithm of the SMAP mission over the tropical and subtropical ocean. GMFs are developed using the collocated statistics of SMAP, CyGNSS, and ARGO ground
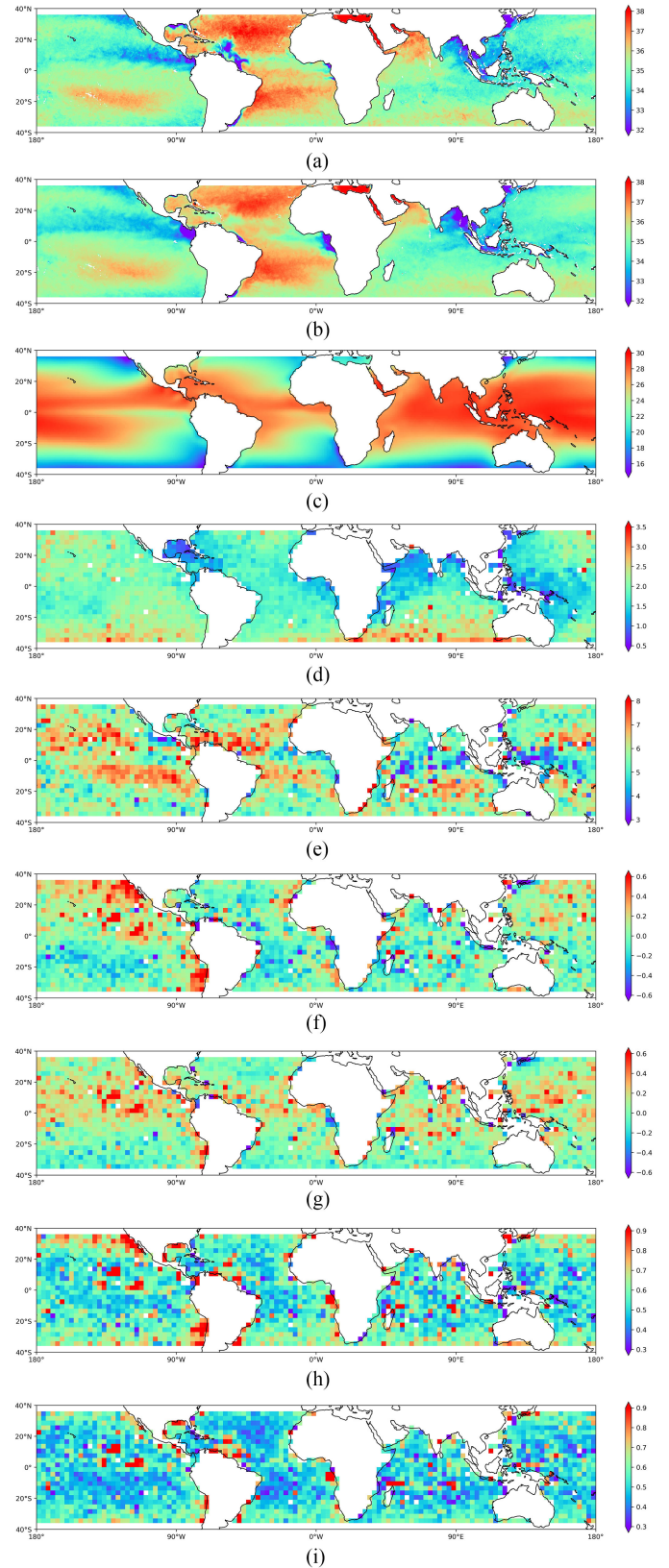

Fig. 11. Spatial variability of SSS uncertainty in $3° \times 3°$ grid. (a) SMAP L3 SSS map in June 2019. (b) SMAP L3 SSS map in January 2020. (c) Long-term mean SST from NOAA. (d) Two-years mean SWH. (e) Two-years mean WS. (f) Bias of SSS_{CYG2}. (g) RMSE of SSS_{CYG2}. (h) Bias of SSS_{v5}. (i) RMSE of SSS_{v5}.

truth. The collocated data sets and new algorithms are implemented in the SMAP SSS retrieval. The improvement can mainly be seen at low WS. In the first decade of satellite ocean salinity, the roughness correction is inaccurate over a smoother ocean, particularly when WS from the weather model is used [28], [38], [54]. When the WS is low, the dependence of excess emissivity on auxiliary WS is weaker [39], [42], and the scattering mechanism cannot reasonably explain experimental observations [38]. The results in this article show that the CyGNSS-assisted SSS retrieval can be 0.1~0.2 psu more accurate than SMAP v5 SSS over the equatorial ocean or at low WS (<2 m/s), which to some extent, proves that GNSS-R could be a new and helpful data source to understand and correct Δe over a smooth ocean. Furthermore, spaceborne GNSS-R is much smaller and cheaper than L-band radiometry. So, as long as it could improve the salinity accuracy in some cases (below 2 m/s), it is worthy of being a hosted payload.

At high WS (> 9 m/s), WS from CyGNSS-like (DDM-based, antenna gain < 15 dB) payload is not accurate enough to be used in SSS retrieval. The large uncertainty (> 0.75 psu) exists even in relatively high antenna gain conditions (RCG > 20). Even if using the CyGNSS-NCEP combined GMF, the reasonable improvement is still only seen at low WS.

Multivariate GMFs are developed and integrated into the SSS retrievals. The dependencies of SSS uncertainties on different geophysical parameters (i.e., SWH, SST, and precipitation) are analyzed. The WS-SWH GMF of CyGNSS differs from the NCEP when WS is high. We speculate that the anomaly on SWH dependence is caused by CyGNSS's insensitivity to the whitecaps. The SST effect correction is based on the "proportional assumption," which is a guess without overwhelming evidence. The $\mathrm{SSS_{v5}}$ and $\mathrm{SSS_{CYG2}}$ overestimated the salinity at high and low SST, respectively. We conclude that the assumption is questionable on a broader SST range. The precipitation dependence of Δe agrees very well with the theoretical knowledge.

The spatial and seasonal variabilities of SSS error are linked to the aforementioned geophysical parameters. The comparisons locate where the current algorithm performs well or poorly. The linkage indicates which parameters are significant in the future GMF development and SSS retrieval.

The findings of this research provide valuable insights for future development and operation of the radiometer-based SSS retrieval algorithm using WS data from spaceborne GNSS-R.

REFERENCES

[1] A. Hasson, M. Puy, J. Boutin, É. Guilyardi, and R. Morrow, "Northward pathway across the tropical North Pacific Ocean revealed by surface salinity: How do El Niño anomalies reach Hawaii?," *J. Geophysical Res., Oceans*, vol. 123, no. 4, pp. 2697–2715, 2018.

[2] C. E. Da Silva and R. M. Castelao, "Mississippi river plume variability in the Gulf of Mexico from SMAP and MODIS—Aqua observations," *J. Geophysical Res., Oceans*, vol. 123, no. 9, pp. 6620–6638, 2018.

[3] J. Boutin, N. Martin, G. Reverdin, X. Yin, and F. Gaillard, "Sea surface freshening inferred from SMOS and ARGO salinity: Impact of rain," *Ocean Sci.*, vol. 9, no. 1, pp. 183–192, 2013.

[4] Y.-C. Liang *et al.*, "Amplified seasonal cycle in hydroclimate over the Amazon river basin and its plume region," *Nature Commun.*, vol. 11, no. 1, 2020, Art. no. 4390.

[5] S. A. Grodsky *et al.*, "Haline hurricane wake in the Amazon/Orinoco plume: AQUARIUS/SACD and SMOS observations," *Geophysical Res. Lett.*, vol. 39, no. 20, 2012, Art. no. L20603.

[6] J. E. Rudzin, L. K. Shay, and W. E. Johns, "The influence of the barrier layer on SST response during tropical cyclone wind forcing using idealized experiments," *J. Phys. Oceanogr.*, vol. 48, no. 7, pp. 1471–1478, 2018.

[7] J. E. Salisbury and B. F. Jönsson, "Rapid warming and salinity changes in the Gulf of Maine alter surface ocean carbonate parameters and hide ocean acidification," *Biogeochemistry*, vol. 141, no. 3, pp. 401–418, 2018.

[8] ARGO, "ARGO float data and metadata from global data assembly centre (ARGO GDAC)," SEANOE, 2020, doi: 10.17882/42182.

[9] N. Reul *et al.*, "Sea surface salinity estimates from spaceborne L-band radiometers: An overview of the first decade of observation (2010–2019)," *Remote Sens. Environ.*, vol. 242, 2020, Art. no. 111769.

[10] L. Klein and C. Swift, "An improved model for the dielectric constant of sea water at microwave frequencies," *IEEE Trans. Antennas Propag.*, vol. 25, no. 1, pp. 104–111, Jan. 1977.

[11] Y. H. Kerr *et al.*, "The SMOS mission: New tool for monitoring key elements of the global water cycle," *Proc. IEEE*, vol. 98, no. 5, pp. 666–687, May 2010.

[12] G. Lagerloef *et al.*, "The Aquarius/SAC-D mission: Designed to meet the salinity remote-sensing challenge," *Oceanography*, vol. 21, no. 1, pp. 68–81, 2008.

[13] T. Meissner, F. J. Wentz, and D. M. Le Vine, "The salinity retrieval algorithms for the NASA Aquarius version 5 and SMAP version 3 releases," *Remote Sens.*, vol. 10, no. 7, 2018, Art. no. 1121.

[14] J. F. Munoz-Martin and A. Camps, "Sea surface salinity and wind speed retrievals using GNSS-R and L-band microwave radiometry data from FMPL-2 onboard the FSSCat mission," *Remote Sens.*, vol. 13, no. 16, 2021, Art. no. 3224.

[15] A. G. Fore, S. H. Yueh, W. Tang, B. W. Stiles, and A. K. Hayashi, "Combined active/passive retrievals of ocean vector wind and sea surface salinity with SMAP," *IEEE Trans. Geosci. Remote Sens.*, vol. 54, no. 12, pp. 7396–7404, Dec. 2016.

[16] S. H. Yueh and J. Chaubell, "Sea surface salinity and wind retrieval using combined passive and active L-band microwave observations," *IEEE Trans. Geosci. Remote Sens.*, vol. 50, no. 4, pp. 1022–1032, Apr. 2012.

[17] D. Entekhabi *et al.*, "The soil moisture active passive (SMAP) mission," *Proc. IEEE*, vol. 98, no. 5, pp. 704–716, May 2010.

[18] C. S. Ruf *et al.*, "New ocean winds satellite mission to probe hurricanes and tropical convection," *Bull. Amer. Meteorological Soc.*, vol. 97, no. 3, pp. 385–395, 2016.

[19] C. Ruf *et al.*, "In-orbit performance of the constellation of CyGNSS hurricane satellites," *Bull. Amer. Meteorological Soc.*, vol. 100, no. 10, pp. 2009–2023, 2019.

[20] S. Zhang, Z. Pu, D. J. Posselt, and R. Atlas, "Impact of CyGNSS ocean surface wind speeds on numerical simulations of a hurricane in observing system simulation experiments," *J. Atmospheric Ocean. Technol.*, vol. 34, no. 2, pp. 375–383, 2017.

[21] C. Chew and E. Small, "Soil moisture sensing using spaceborne GNSS reflections: Comparison of CyGNSS reflectivity to SMAP soil moisture," *Geophysical Res. Lett.*, vol. 45, no. 9, pp. 4049–4057, 2018.

[22] Q. Yan, W. Huang, S. Jin, and Y. Jia, "Pan-tropical soil moisture mapping based on a three-layer model from CyGNSS GNSS-R data," *Remote Sens. Environ.*, vol. 247, 2020, Art. no. 111944.

[23] M. P. Clarizia, N. Pierdicca, F. Costantini, and N. Floury, "Analysis of CyGNSS data for soil moisture retrieval," *IEEE J. Sel. Topics Appl. Earth Observ. Remote Sens.*, vol. 12, no. 7, pp. 2227–2235, Jul. 2019.

[24] M. M. Al-Khaldi, J. T. Johnson, A. J. O'Brien, A. Balenzano, and F. Mattia, "Time-series retrieval of soil moisture using CyGNSS," *IEEE Trans. Geosci. Remote Sens.*, vol. 57, no. 7, pp. 4322–4331, Jul. 2019.

[25] C. Chew and E. Small, "Estimating inundation extent using CyGNSS data: A conceptual modeling study," *Remote Sens. Environ.*, vol. 246, 2020, Art. no. 111869.

[26] W. Li, E. Cardellach, F. Fabra, S. Ribo, and A. Rius, "Lake level and surface topography measured with spaceborne GNSS-reflectometry from CyGNSS mission: Example for the Lake Qinghai," *Geophysical Res. Lett.*, vol. 45, no. 24, pp. 13332–13341, 2018.

[27] W. Li, E. Cardellach, F. Fabra, S. Ribó, and A. Rius, "Assessment of spaceborne GNSS-R ocean altimetry performance using CyGNSS mission raw data," *IEEE Trans. Geosci. Remote Sens.*, vol. 58, no. 1, pp. 238–250, Jan. 2020.

[28] B. Liu, W. Wan, and Y. Hong, "Can the accuracy of sea surface salinity measurement be improved by incorporating spaceborne GNSS-Reflectometry?," *IEEE Geosci. Remote Sens. Lett.*, vol. 18, no. 1, pp. 3–7, Jan. 2021.

[29] R. Sabia, M. Caparrini, A. Camps, and G. Ruffini, "Potential synergetic use of GNSS-R signals to improve the sea-state correction in the sea surface salinity estimation: Application to the SMOS mission," *IEEE Trans. Geosci. Remote Sens.*, vol. 45, no. 7, pp. 2088–2097, Jul. 2007.

[30] E. Valencia *et al.*, "Improving the accuracy of sea surface salinity retrieval using GNSS-R data to correct the sea state effect," *Radio Sci.*, vol. 46, no. 6, pp. 1–11, 2011.

[31] V. U. Zavorotny and A. G. Voronovich, "Scattering of GPS signals from the ocean with wind remote sensing application," *IEEE Trans. Geosci. Remote Sens.*, vol. 38, no. 2, pp. 951–964, Mar. 2000.

[32] F. Said, Z. Jelenak, J. Park, and P. S. Chang, "The NOAA track-wise wind retrieval algorithm and product assessment for CyGNSS," *IEEE Trans. Geosci. Remote Sens.*, to be published, doi: 10.1109/TGRS.2021.3087426.

[33] M. P. Clarizia and C. S. Ruf, "Wind speed retrieval algorithm for the cyclone global navigation satellite system (CyGNSS) mission," *IEEE Trans. Geosci. Remote Sens.*, vol. 54, no. 8, pp. 4419–4432, Aug. 2016.

[34] NOAA/NESDIS/STAR/SOCD, 2020, "CyGNSS level 2 climate data record version 1.1," PO.DAAC, CA, USA, doi: 10.5067/CYGNS-L2C11.

[35] NASA/JPL, 2020, "JPL SMAP level 2B CAP sea surface salinity V5.0 validated dataset," PO.DAAC, CA, USA, doi: 10.5067/SMP50-2TOCS.

[36] E. Oka and K. Ando, "Stability of temperature and conductivity sensors of ARGO profiling floats," *J. Oceanogr.*, vol. 60, no. 2, pp. 253–258, 2004.

[37] G. J. Huffman, D. T. Bolvin, and E. J. Nelkin, *Integrated Multi-SatellitE Retrievals for GPM (IMERG) Technical Documentation*. Greenbelt, MD, USA: NASA/GSFC, 2015.

[38] S. H. Yueh *et al.*, "L-band passive and active microwave geophysical model functions of ocean surface winds and applications to Aquarius retrieval," *IEEE Trans. Geosci. Remote Sens.*, vol. 51, no. 9, pp. 4619–4632, Sep. 2013.

[39] T. Meissner, F. J. Wentz, and L. Ricciardulli, "The emission and scattering of L-band microwave radiation from rough ocean surfaces and wind speed measurements from the Aquarius sensor," *J. Geophysical Res., Oceans*, vol. 119, no. 9, pp. 6499–6522, 2014.

[40] C. S. Ruf *et al.*, *CyGNSS Handbook*. Ann Arbor, MI, USA: Michigan Publishing, 2016.

[41] M. P. Clarizia, C. S. Ruf, P. Jales, and C. Gommenginger, "Spaceborne GNSS-R minimum variance wind speed estimator," *IEEE Trans. Geosci. Remote Sens.*, vol. 52, no. 11, pp. 6829–6843, Nov. 2014.

[42] A. Camps *et al.*, "The WISE 2000 and 2001 field experiments in support of the SMOS mission: Sea surface L-band brightness temperature observations and their application to sea surface salinity retrieval," *IEEE Trans. Geosci. Remote Sens.*, vol. 42, no. 4, pp. 804–823, Apr. 2004.

[43] T. Meissner, L. Ricciardulli, and F. J. Wentz, "Capability of the SMAP mission to measure ocean surface winds in storms," *Bull. Amer. Meteorological Soc.*, vol. 98, no. 8, pp. 1660–1677, 2017.

[44] C. S. Ruf and R. Balasubramaniam, "Development of the CyGNSS geophysical model function for wind speed," *IEEE J. Sel. Topics Appl. Earth Observ. Remote Sens.*, vol. 12, no. 1, pp. 66–77, Jan. 2019.

[45] M. J. D. Powell, "A direct search optimization method that models the objective and constraint functions by linear interpolation," in *Advances in Optimization and Numerical Analysis*, S. Gomez and J.-P. Hennart, Eds., Dordrecht, The Netherlands: Springer, 1994, pp. 51–67.

[46] A. G. Voronovich and V. U. Zavorotny, "The transition from weak to strong diffuse radar bistatic scattering from rough ocean surface," *IEEE Trans. Antennas Propag.*, vol. 65, no. 11, pp. 6029–6034, Nov. 2017.

[47] B. Li, L. Yang, B. Zhang, D. Yang, and D. Wu, "Modeling and simulation of GNSS-R observables with effects of swell," *IEEE J. Sel. Topics Appl. Earth Observ. Remote Sens.*, vol. 13, pp. 1833–1841, 2020.

[48] M. P. Clarizia and C. S. Ruf, "Bayesian wind speed estimation conditioned on significant wave height for GNSS-R ocean observations," *J. Atmospheric Ocean. Technol.*, vol. 34, no. 6, pp. 1193–1202, 2017.

[49] X. Yin, J. Boutin, N. Martin, P. Spurgeon, J. L. Vergely, and F. Gaillard, "Errors in SMOS sea surface salinity and their dependency on a priori wind speed," *Remote Sens. Environ.*, vol. 146, pp. 159–171, 2014.

[50] J. Boutin *et al.*, "New SMOS sea surface salinity with reduced systematic errors and improved variability," *Remote Sens. Environ.*, vol. 214, pp. 115–134, 2018.

[51] N. Sharma, "Retrieval of sea surface salinity from SMAP L-band radiometer: A novel approach for wind speed correction," *Quart. J. Roy. Meteorological Soc.*, vol. 145, no. 725, pp. 3455–3465, 2019.

[52] W. Tang, S. H. Yueh, A. Fore, G. Neumann, A. Hayashi, and G. Lagerloef, "The rain effect on Aquarius' L-band sea surface brightness temperature and radar backscatter," *Remote Sens. Environ.*, vol. 137, pp. 147–157, 2013.

[53] J. Boutin *et al.*, "Satellite and in situ salinity: Understanding near-surface stratification and subfootprint variability," *Bull. Amer. Meteorological Soc.*, vol. 97, no. 8, pp. 1391–1407, 2016.

[54] J. Boutin, N. Martin, X. Yin, J. Font, N. Reul, and P. Spurgeon, "First assessment of SMOS data over open ocean: Part II—Sea surface salinity," *IEEE Trans. Geosci. Remote Sens.*, vol. 50, no. 5, pp. 1662–1675, May 2012.

Baojian Liu received the B.S. degree in geographic information science in 2017 from the School of Earth and Space Science, Peking University, Beijing, China, where he is currently working toward the Ph.D. degree in photogrammetry and remote sensing.

His research interests include GNSS-reflectometry remote sensing and hydrological remote sensing.

Wei Wan received the M.E. degree from Nanjing University, Nanjing, China, in 2010 and the Ph.D. degree from Peking University, Beijing, China, in 2014, both in photogrammetry and remote sensing.

She is currently an Assistant Research Fellow with the Institute of Remote Sensing and GIS, Peking University. From 2014 to 2017, she worked as a Postdoctoral Researcher with Tsinghua University. Her research interests include GNSS remote sensing and satellite remote sensing of lakes and reservoirs.

Zhizhou Guo received the B.S. degree in geographic information science in 2021 from the School of Earth and Space Science, Peking University, Beijing, China, where he is currently working toward the Ph.D. degree in photogrammetry and remote sensing.

His research interests cover GNSS remote sensing and hydrological remote sensing.

Rui Ji received the B.S. degree in geographic information science in 2019 from the School of Earth and Space Sciences, Peking University, Beijing, China, where he is currently working toward the Ph.D. degree in photogrammetry and remote sensing.

His research interests include remote sensing big data, remote sensing image processing, and deep learning.

Tsechun Wang received the B.S. degree in geomatics from the Department of Geomatics, National Cheng Kung University, Tainan, Taiwan, in 2016 and the M.S. degree in geographic information science from the Department of Civil Engineering, National Central University, Taoyuan, Taiwan, in 2018. He is currently working toward the Ph.D. degree in photogrammetry and remote sensing from the School of Earth and Space Science, Peking University, Beijing, China.

His research interests include remote sensing big data, remote sensing of extreme precipitation.

Yaokui Cui received the B.S. degree in remote sensing science and technology from the School of Remote Sensing and Information Engineering, Wuhan University, Wuhan, China, in 2008, the M.S. degree in photogrammetry and remote sensing from the School of Earth and Space Science, Peking University, Beijing, China, in 2011, and the Ph.D. degree in science from the Institute of Remote Sensing and Digital Earth, Chinese Academy of Sciences, Beijing, China, in 2015.

He is currently with the Institute of Remote Sensing and GIS, School of Earth and Space Sciences, Peking University, Beijing, China. His current research interests focus on remote sensing evapotranspiration, soil moisture, and remote sensing big data.

Guoqiang Tang received the B.S. degree from the Department of Hydraulic Engineering, Tsinghua University, Beijing, China, in 2014, and the Ph.D. degree from the Department of Hydraulic Engineering, Tsinghua University, Beijing, China, in 2019.

He is currently a Postdoc with the University of Saskatchewan, Saskatoon, SK, Canada. His research interests include remote sensing and precipitation, probabilistic meteorological datasets, large-scale hydrology, and deep learning techniques.

Yang Hong received the Ph.D. degree with a major in hydrology and water resources and minor in remote sensing and spatial analysis from the University of Arizona, Tucson, AZ, USA.

His primary research interests are in hydrology and water resources, natural hazard prediction, land surface modeling, and data assimilation systems for water resource planning under changing climate.